Supporting Information for

MOF-derived 1D hollow bimetallic iron(III) oxide nanorods: Effects of metal-addition on the phase transition, morphology and magnetic properties

Junhyung Lee[a,b*]

[a]ECA, Korea Advanced Nano Fab Center, 109, Gwanggyo-ro, Yeongtong-gu, Suwon-si, Gyeonggi-do, 16229, Korea

[b]Department of Materials Science and Engineering, Seoul National University, 1 Gwanak-ro, Gwanak-gu, Seoul 08826, Korea

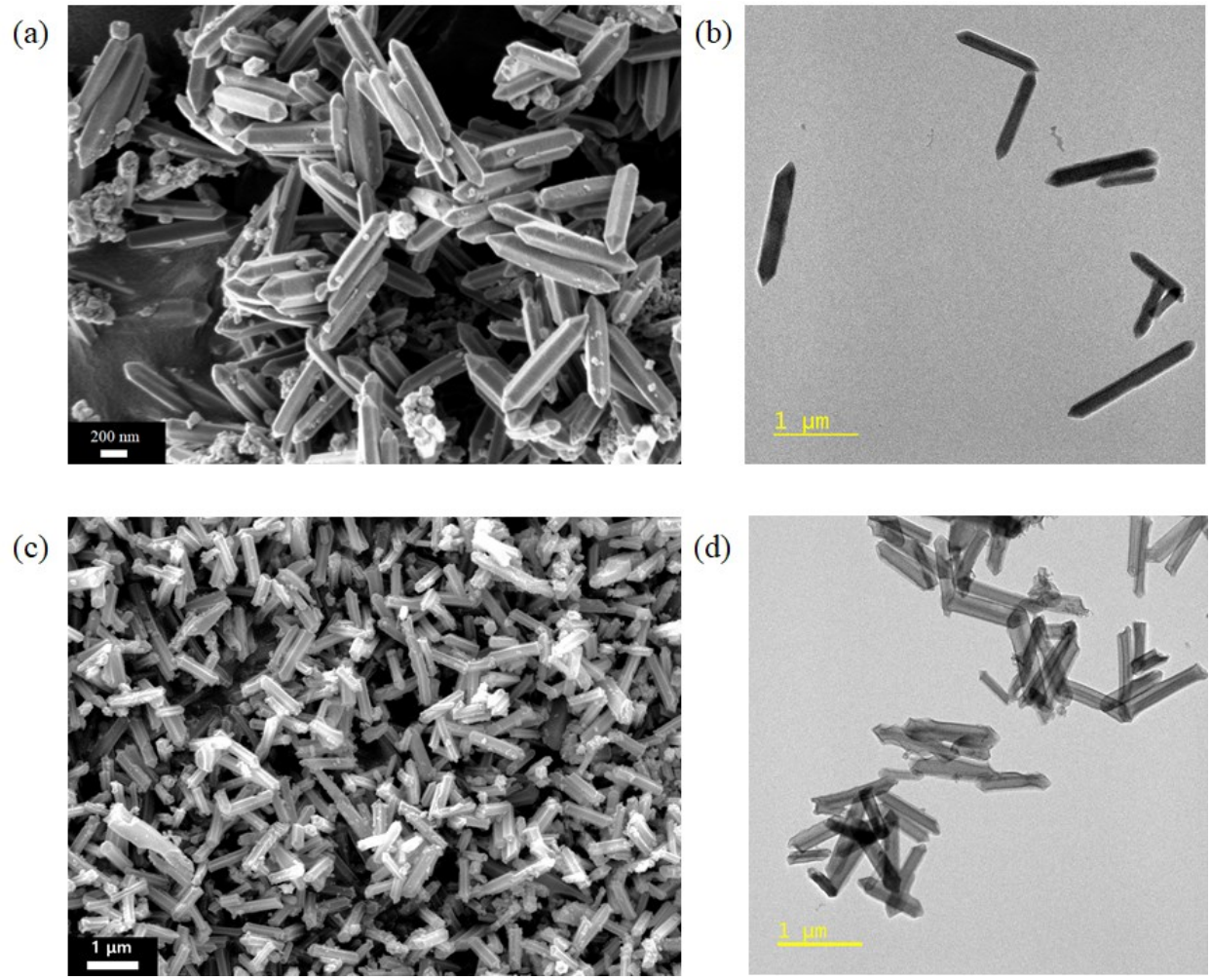

Fig. S1. (a) SEM and (b) TEM images of MIL-88A; (c) SEM and (d) TEM images of MIL-88A etched by NH_4OH

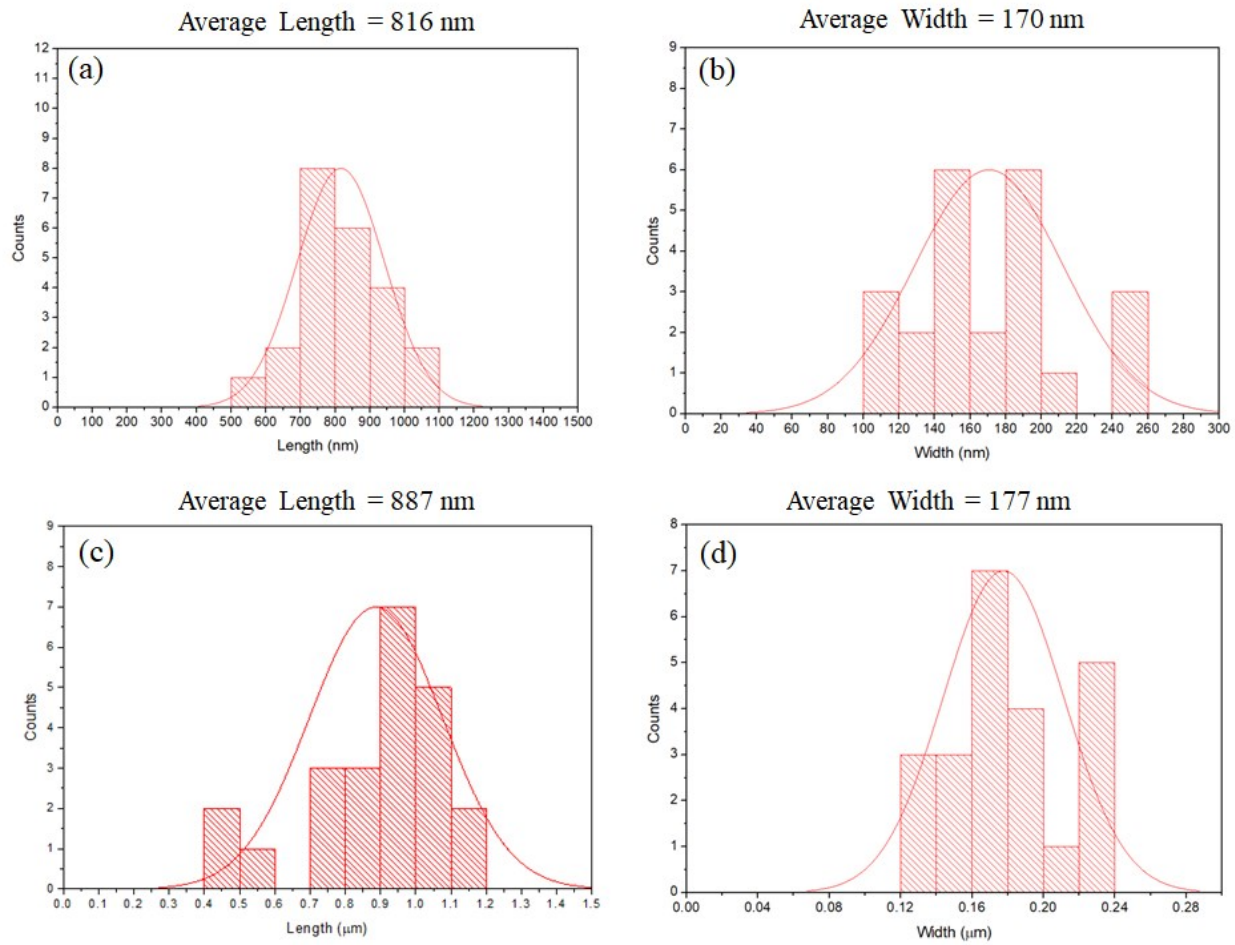

Fig. S1-2. The average length and width of (a, b) Fe-MIL-88A (c, d) NH_4OH-MOF

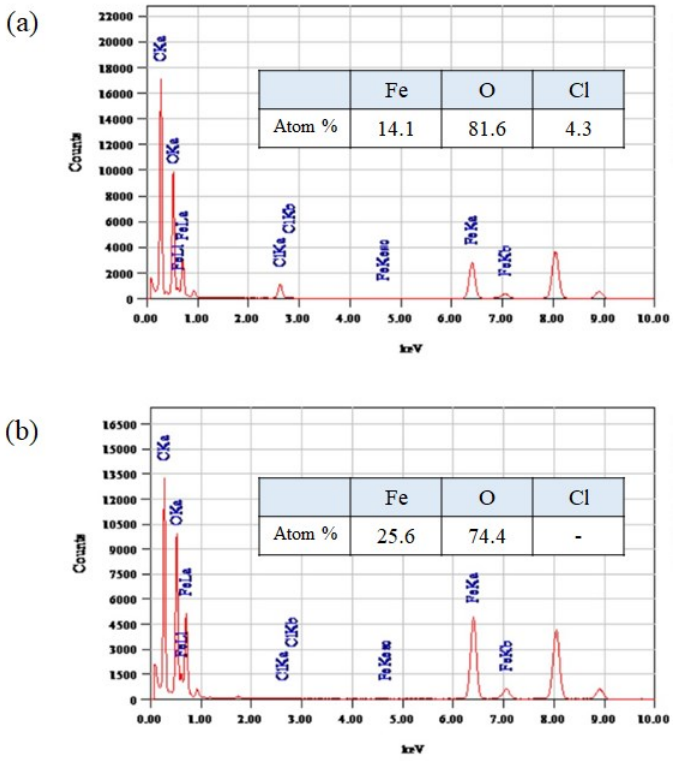

Fig. S2. EDS spectra of (a) Fe-MIL-88A and (b) NH_4OH-MOF

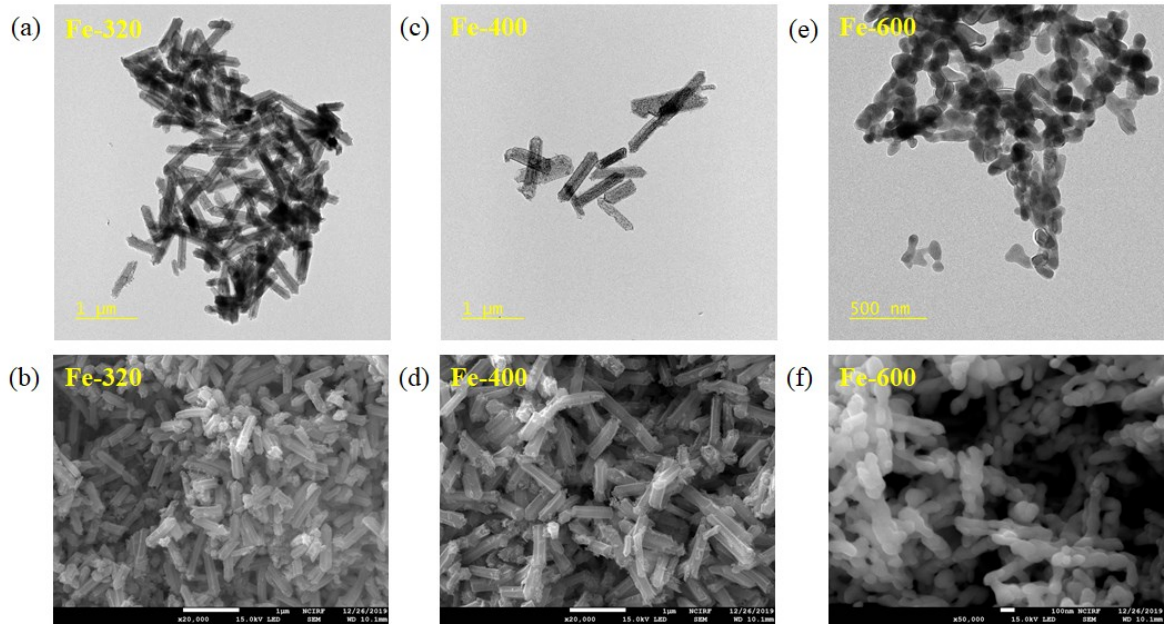

Fig. S3. TEM and SEM images of (a, b) Fe-320 (c, d) Fe-400 (e, f) Fe-600

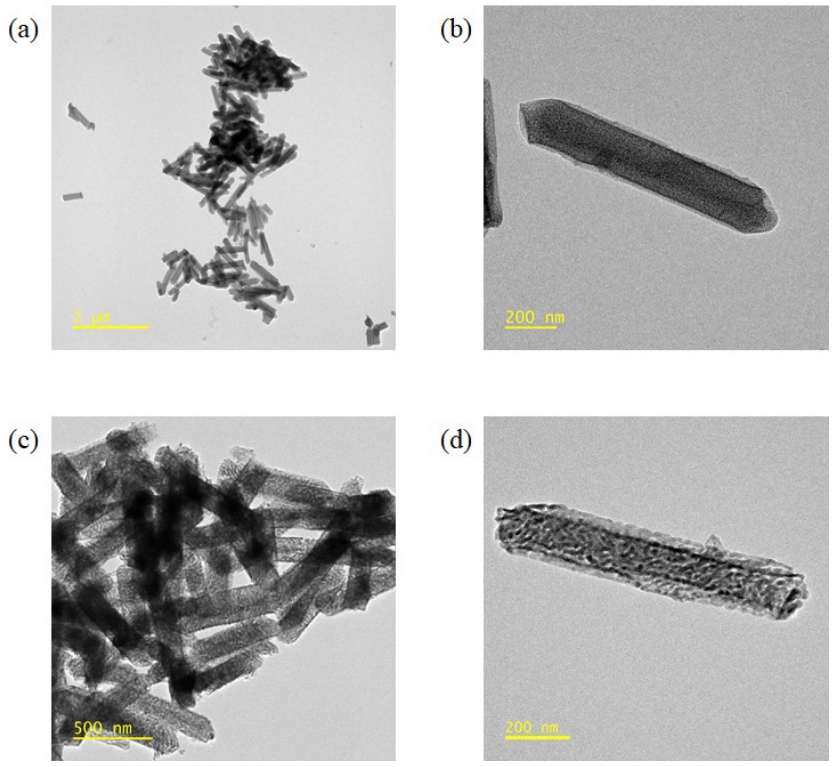

Fig. S4. TEM images of (a, b) MnFe-320 and (c, d) MnFe-400

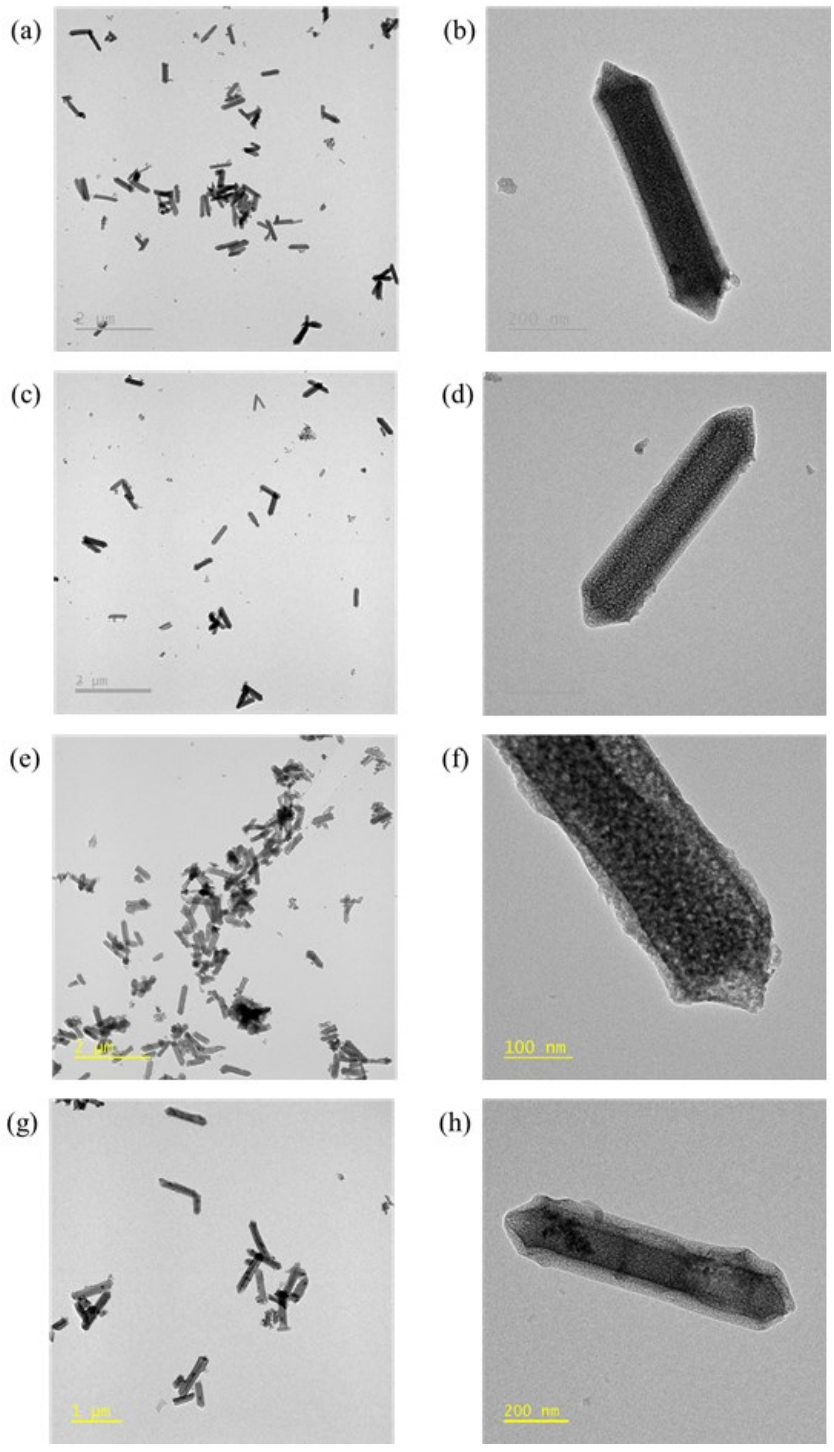

Fig. S5. TEM images of (a, b) NiFe-400 (c, d) LaFe-400 (e, f) RuFe-320 (g, h) AgFe-400

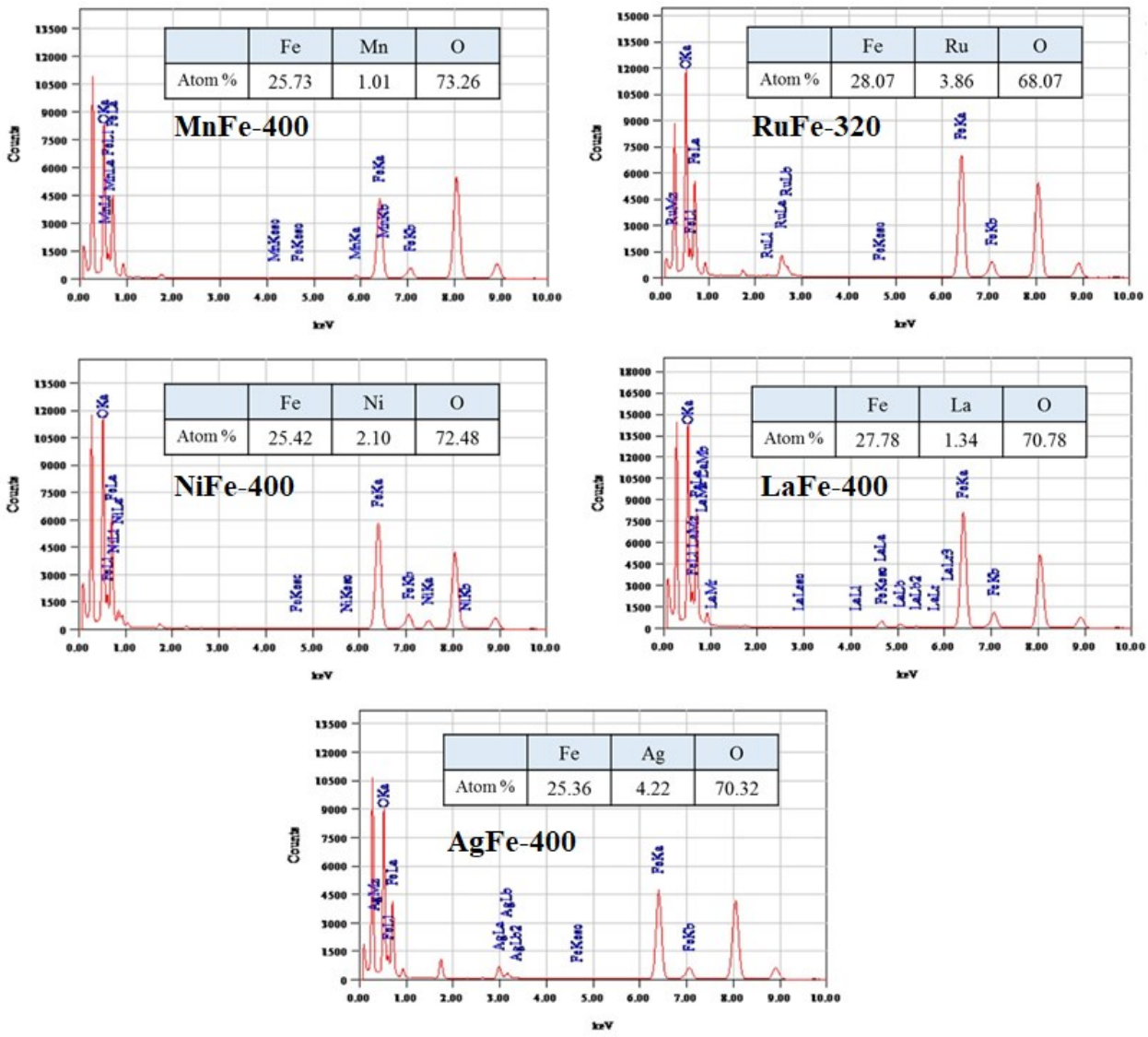

Fig. S6. EDS spectra of prepared 1D hollow bimetallic iron oxide nanorods.

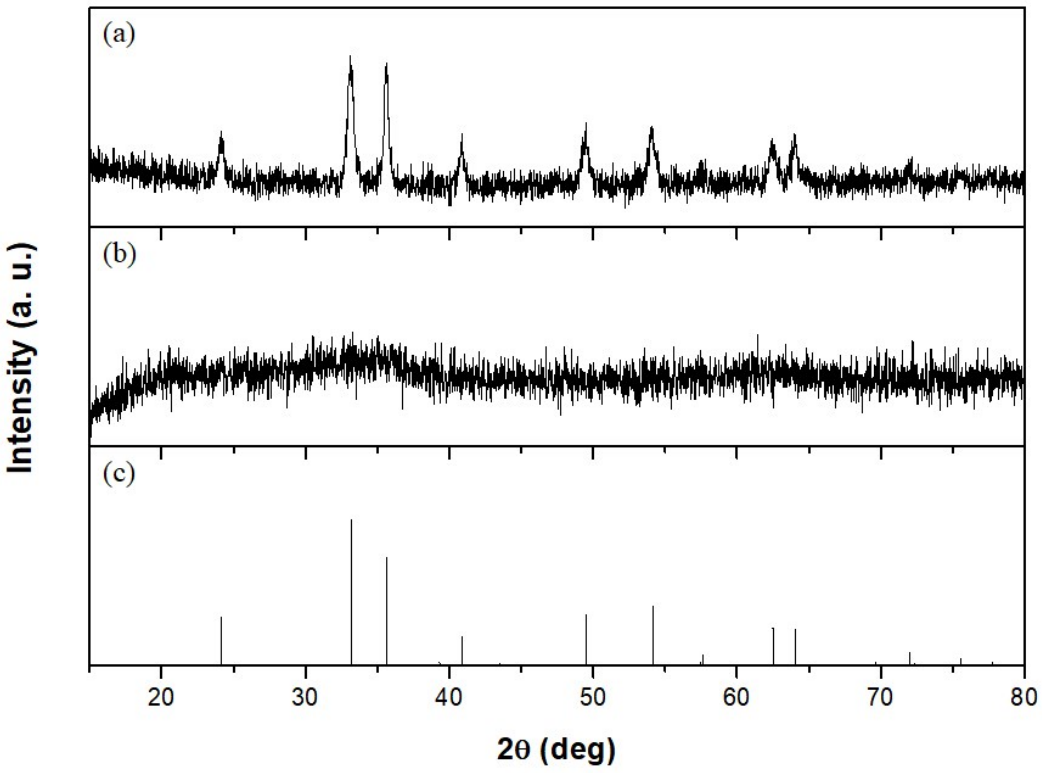

Fig. S7. XRD patterns of (a) MnFe-400 (b) MnFe-320 and (c) α-Fe_2O_3 (ICDD No. 04-006-6579)

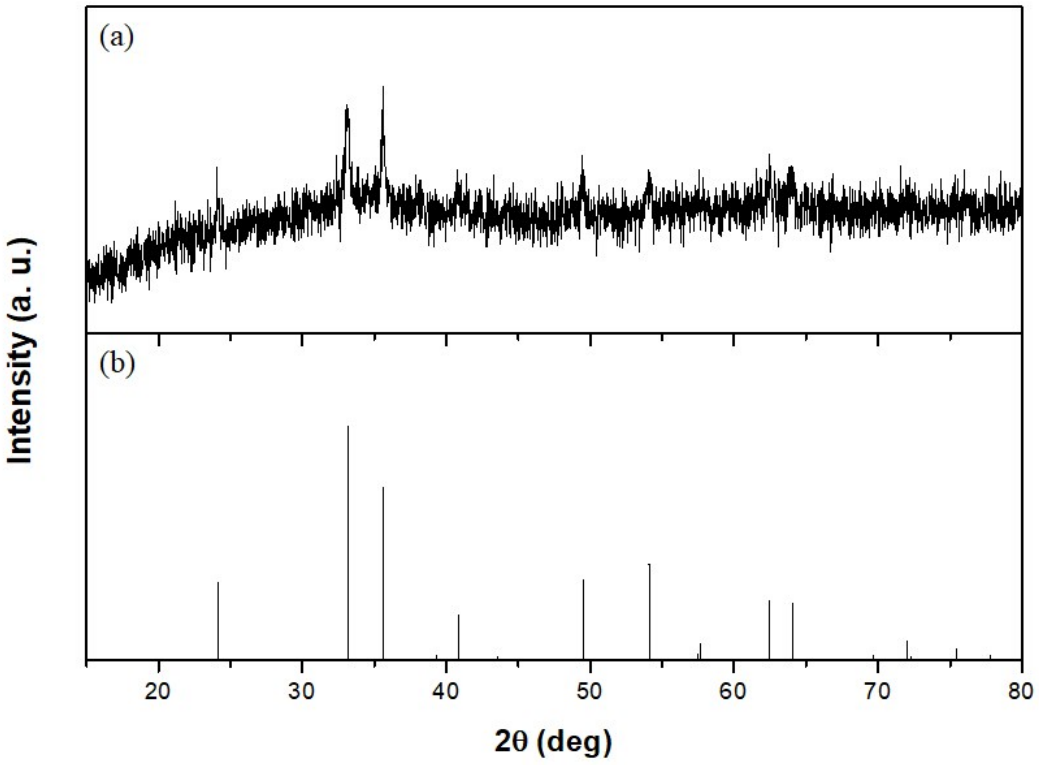

Fig. S8. XRD patterns of (a) AgFe-400 and (b) simulated α-Fe_2O_3 (ICDD No. 04-006-6579)

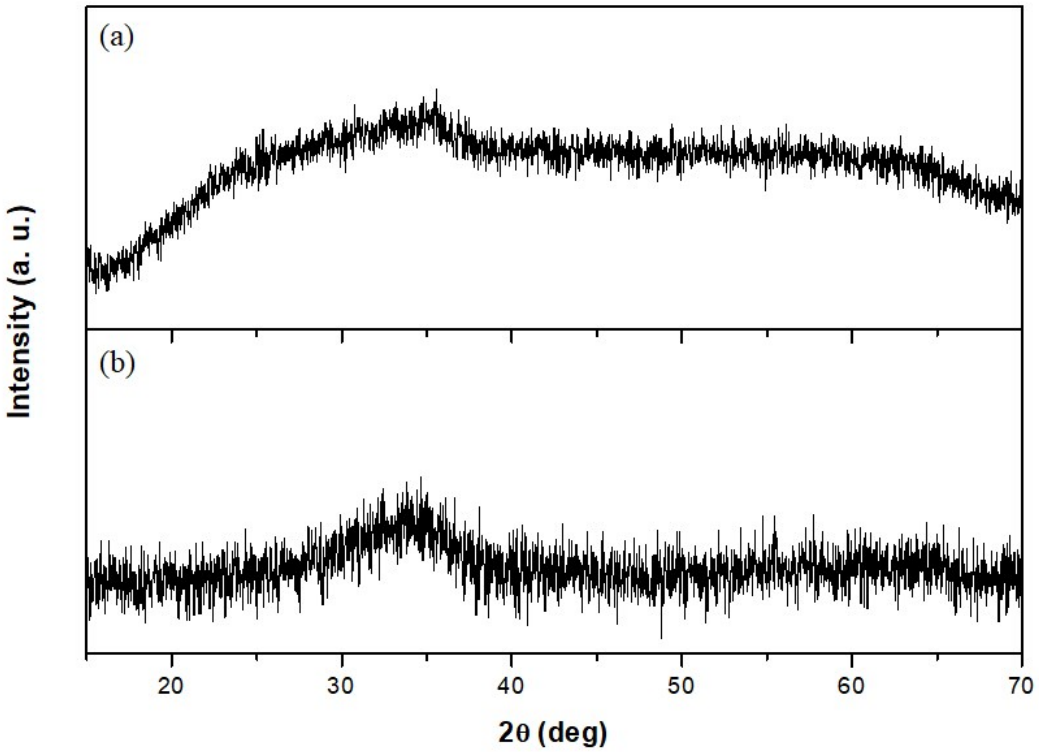

Fig. S9. XRD patterns of (a) LaFe-500 and (b) LaFe-400

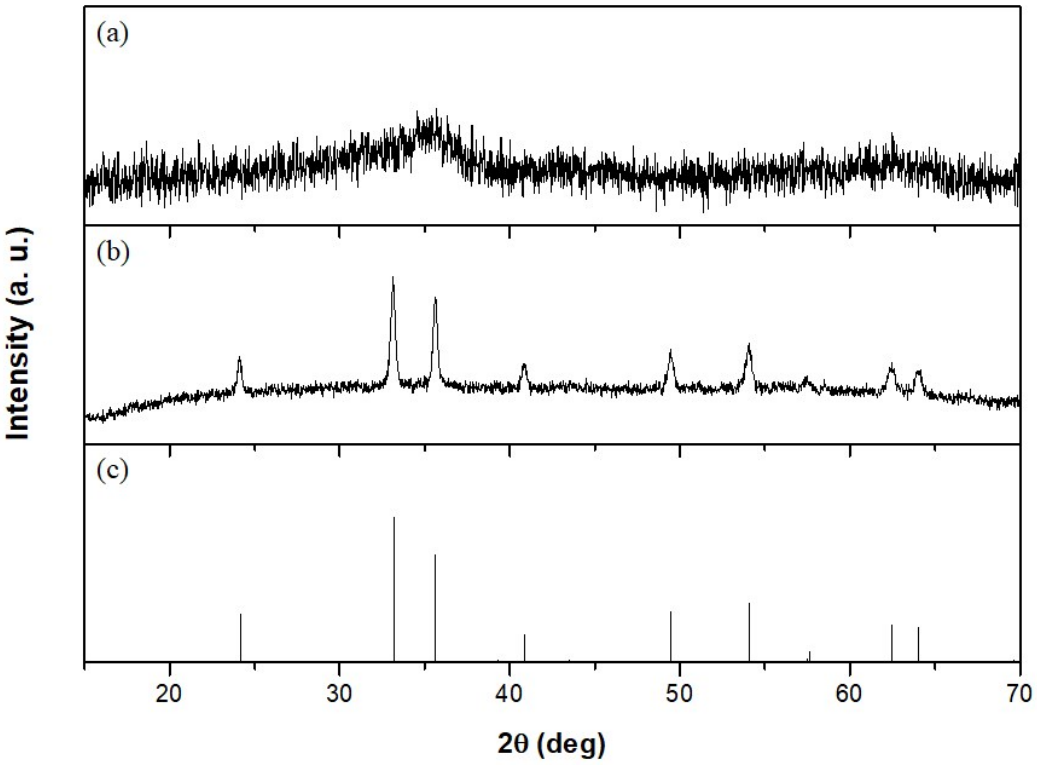

Fig. S10. XRD patterns of (a) NiFe-400 (b) NiFe-500 and (c) α-Fe_2O_3 (ICDD No. 04-006-6579)

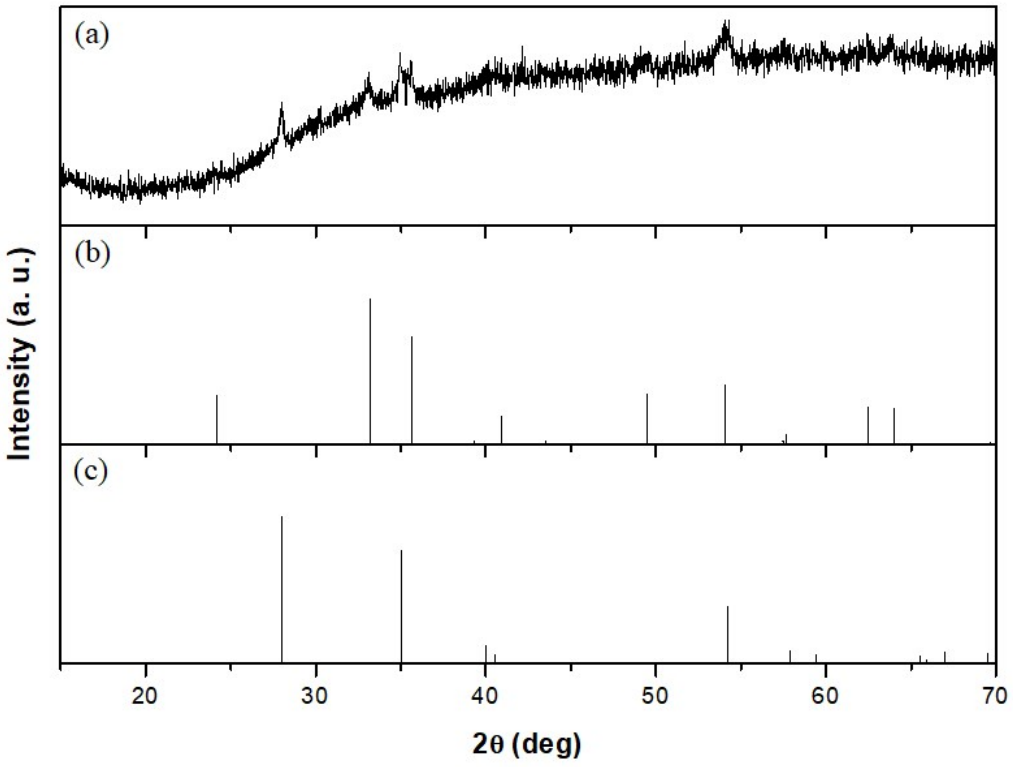

Fig. S11. XRD patterns of (a) RuFe-320 (b) α-Fe_2O_3 (ICDD No. 04-006-6579) and (c) RuO_2 (ICDD No. 00-040-1290)

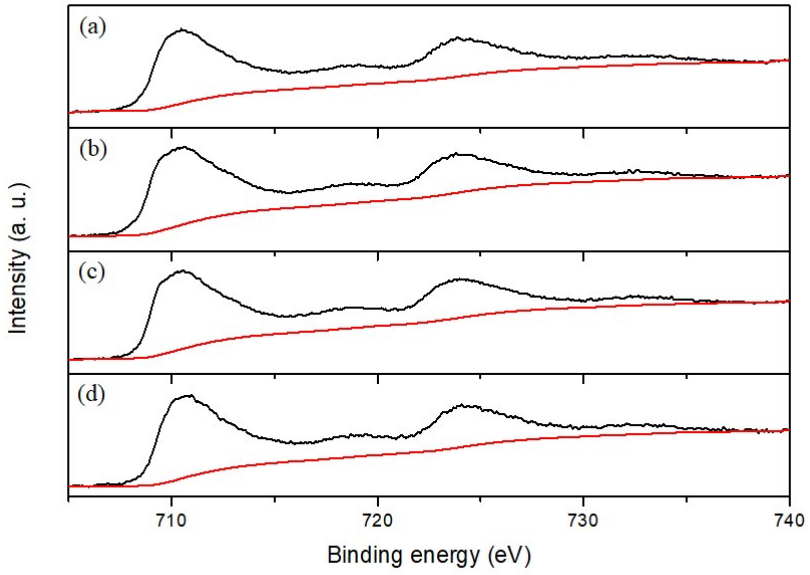

Fig. S12. XPS spectra of Fe 2p for the (a) NiFe-400 (b) RuFe-320 (c) AgFe-400 and (d) LaFe-400

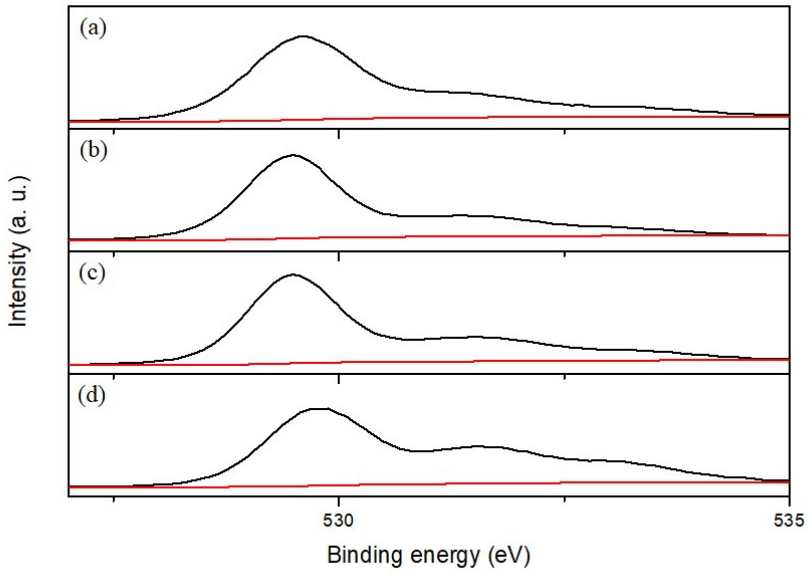

Fig. S13. XPS spectra of O 1s for the (a) NiFe-400 (b) RuFe-320 (c) AgFe-400 and (d) LaFe-400

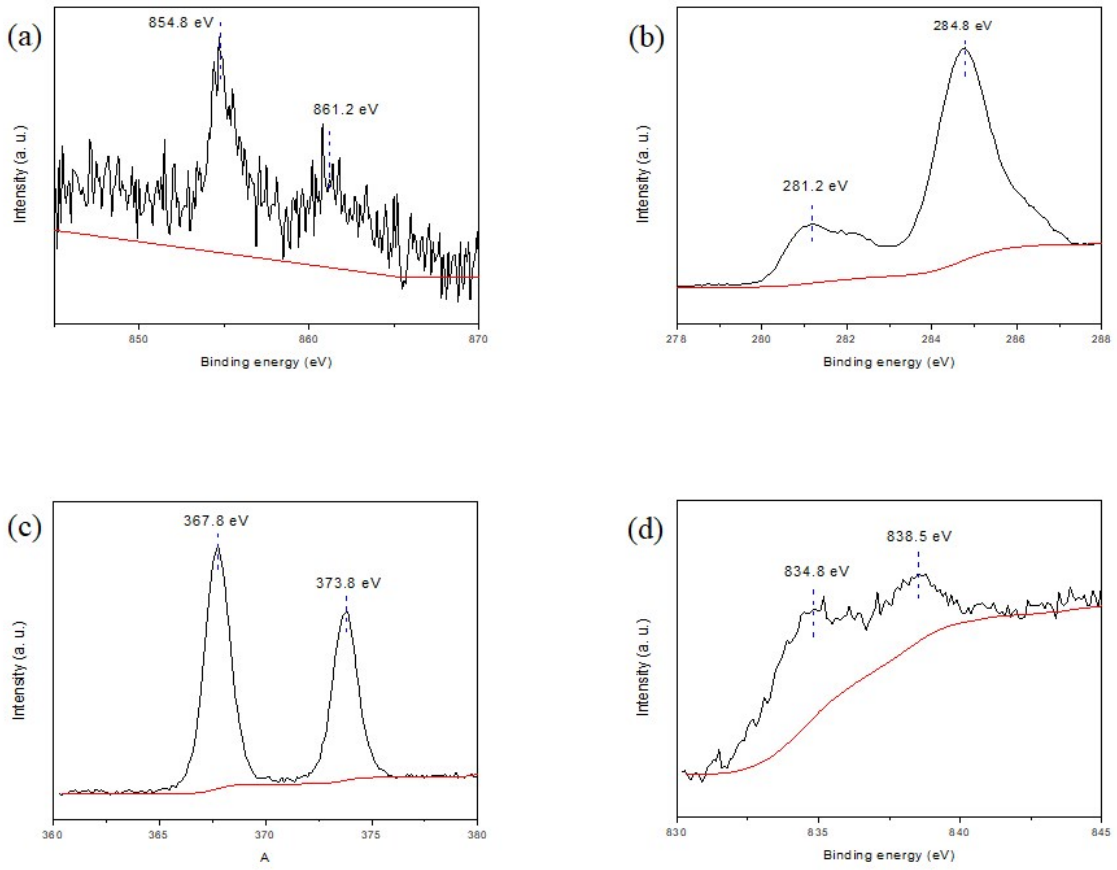

Fig. S14. XPS spectra of (a) Ni 2p of NiFe-400 (b) Ru 3d of RuFe-320 (c) Ag of AgFe-400 and (d) La of LaFe-400

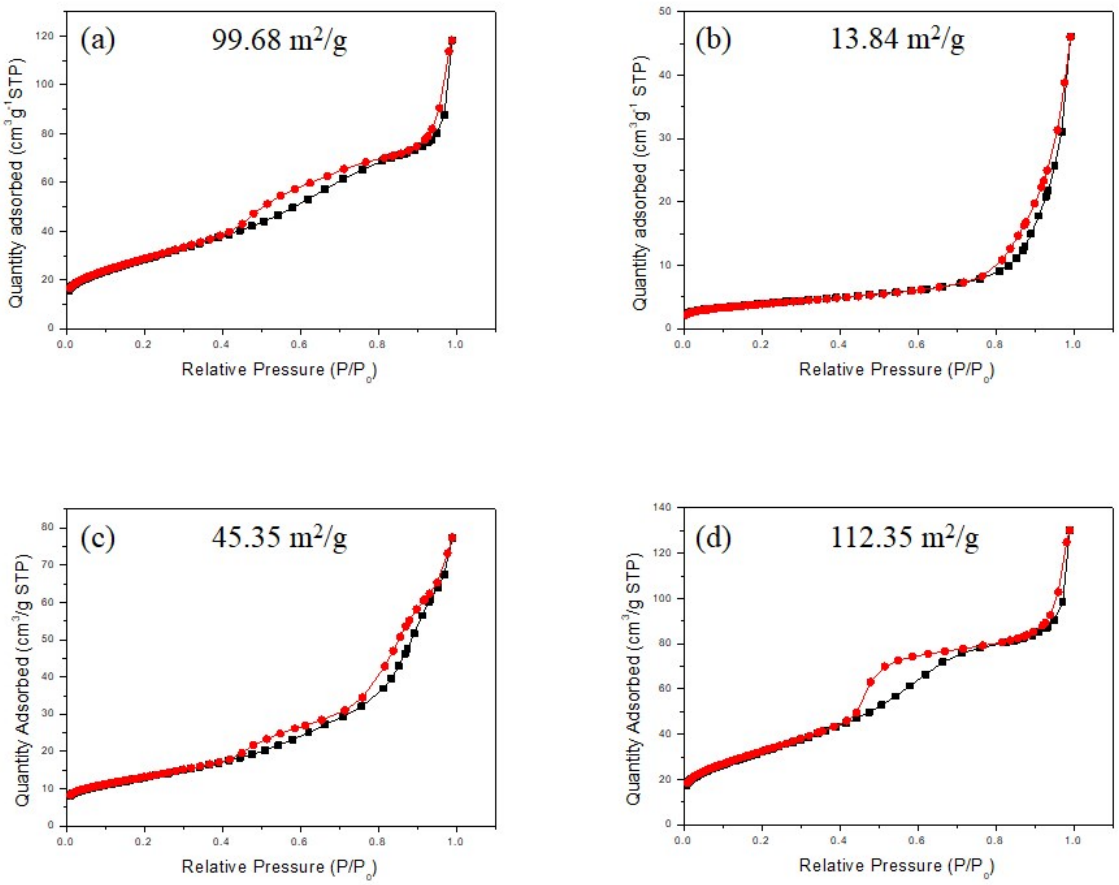

Fig. S15. N_2 adsorption-desorption isotherm of (a) NiFe-400 (b) RuFe-320 (c) AgFe-400 and (d) LaFe-400

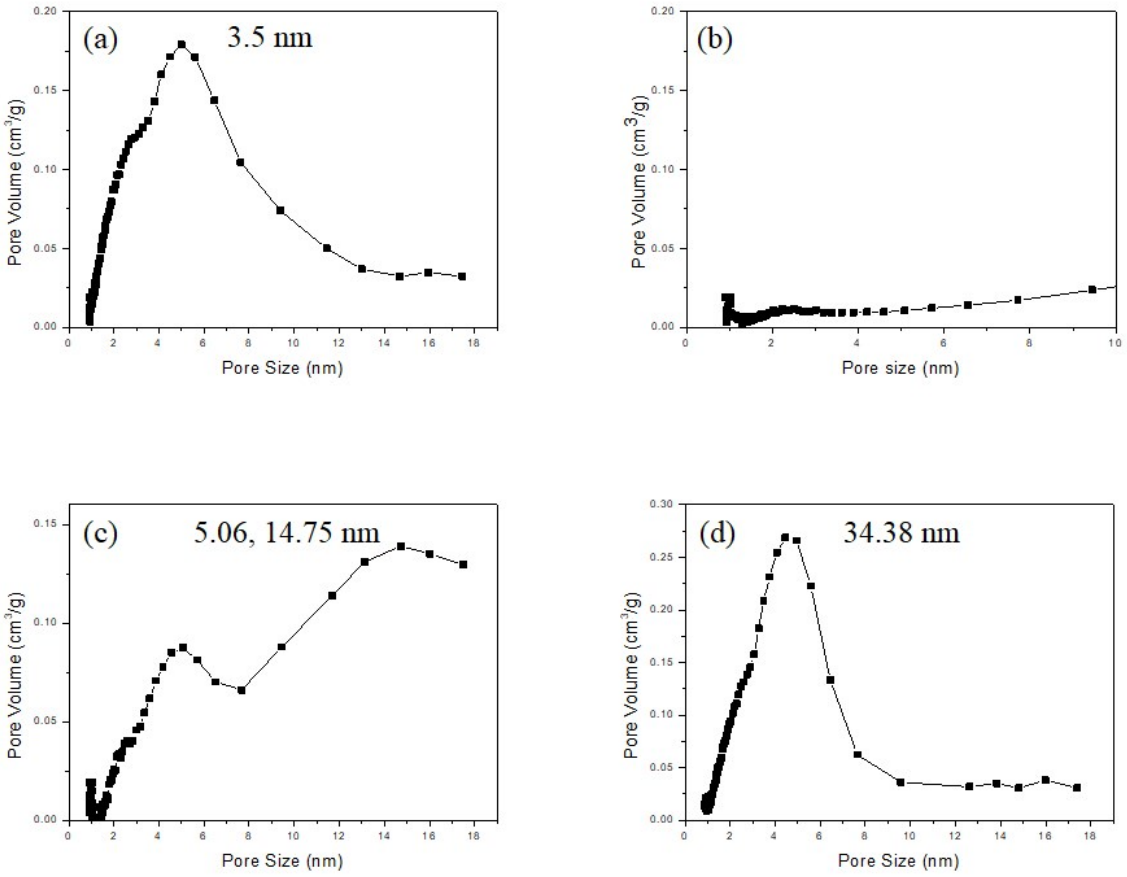

Fig. S16. The pore size distribution of (a) NiFe-400 (b) RuFe-320 (c) AgFe-400 and (d) LaFe-400

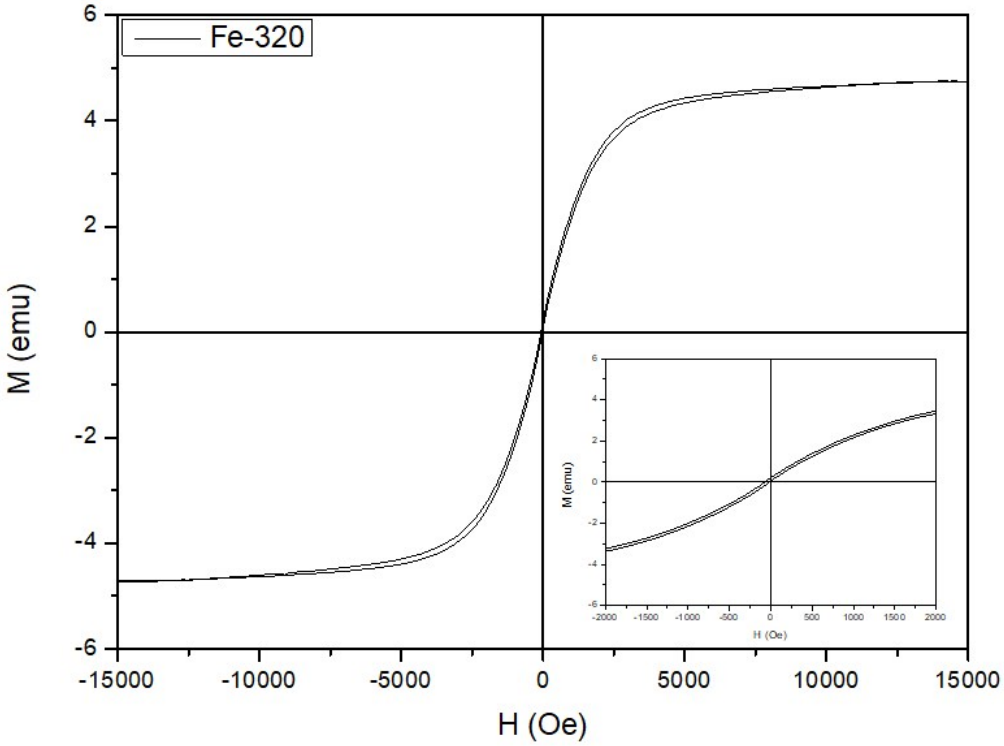

Fig. S17. Magnetic hysteresis loops of Fe-320

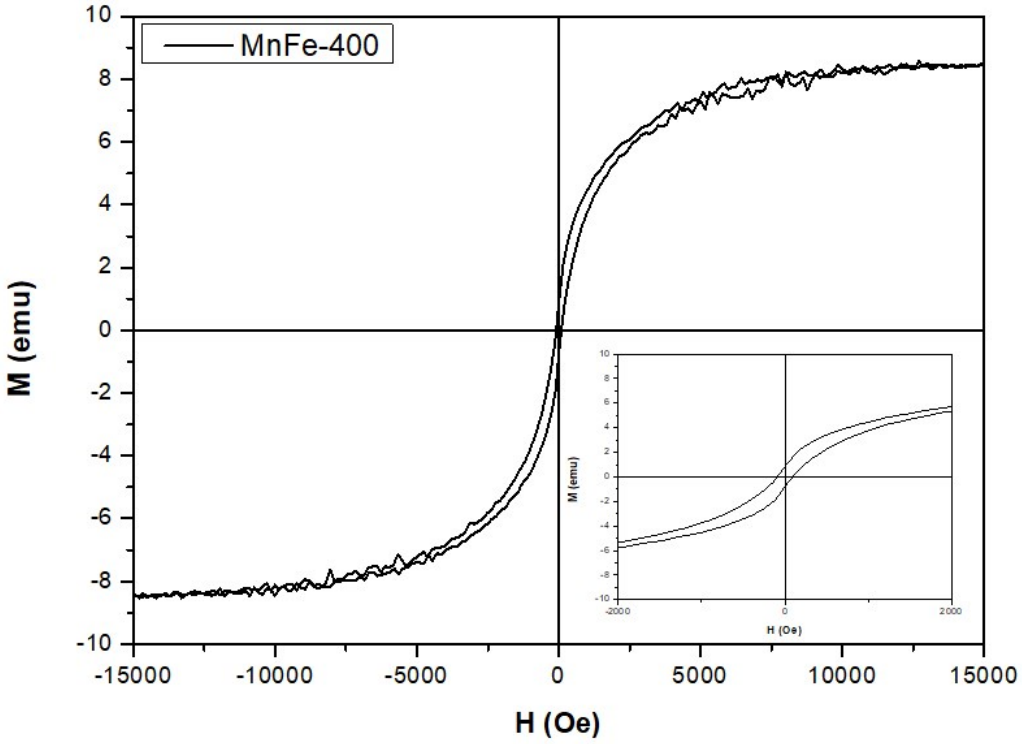

Fig. S18. Magnetic hysteresis loops of MnFe-400

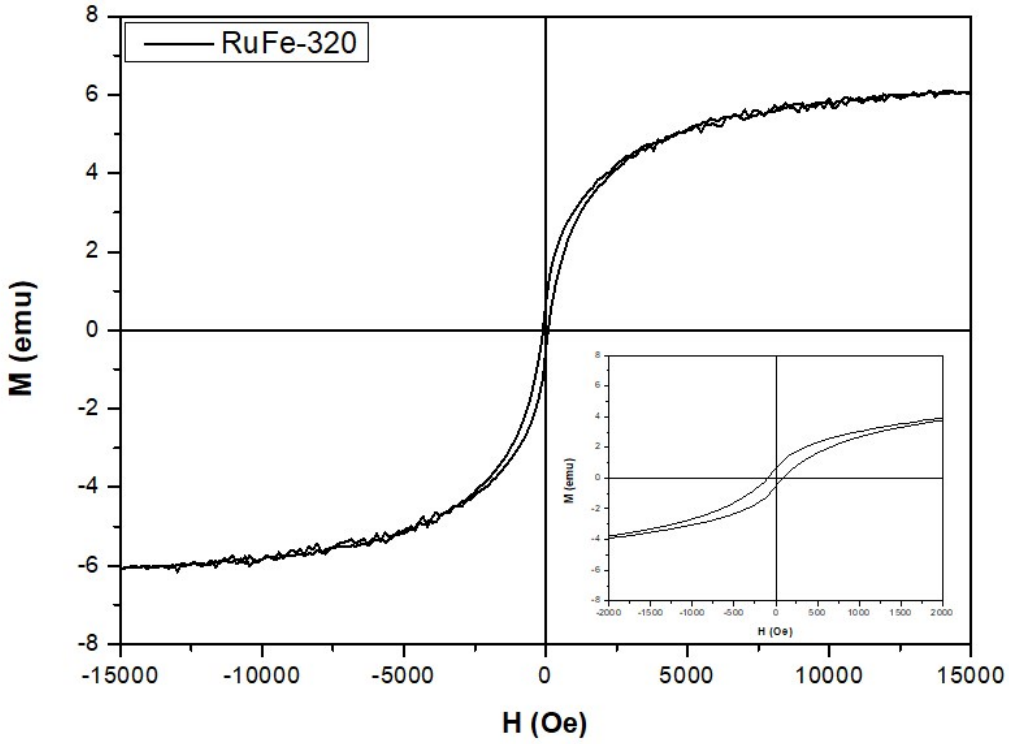

Fig. S19. Magnetic hysteresis loops of RuFe-320

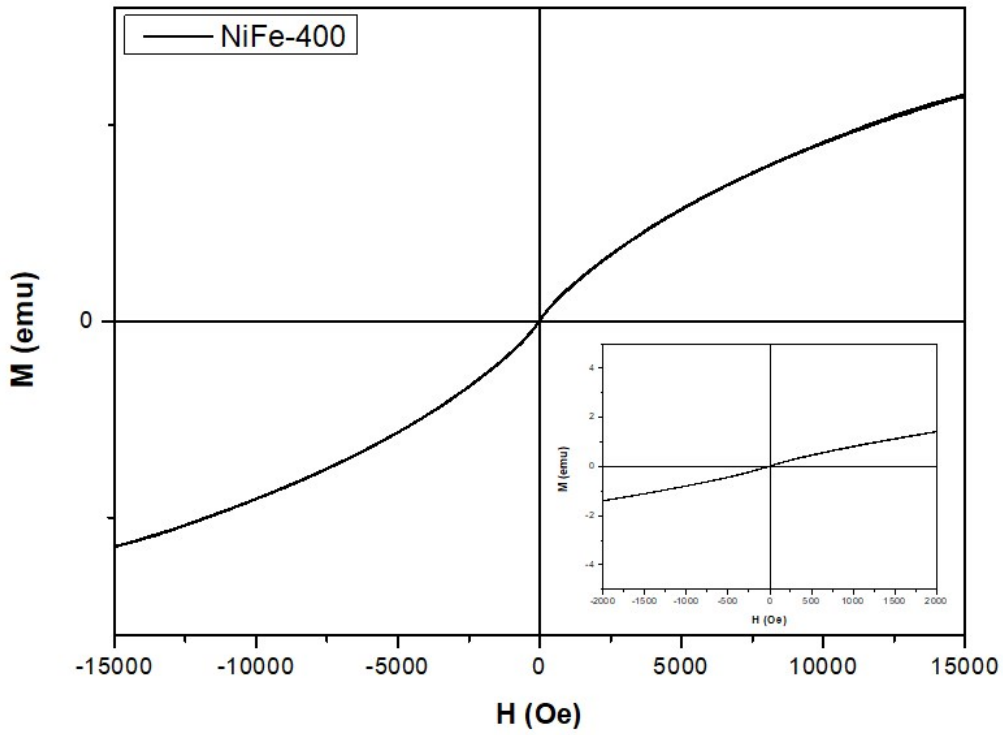

Fig. S20. Magnetic hysteresis loops of NiFe-400

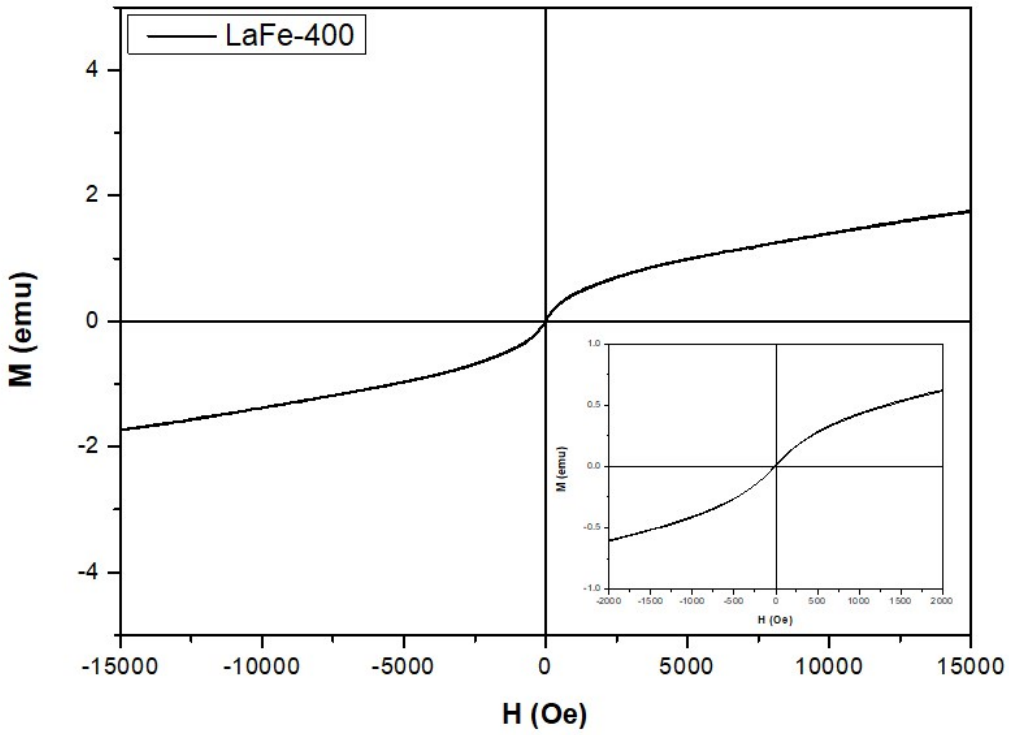

Fig. S21. Magnetic hysteresis loops of LaFe-400

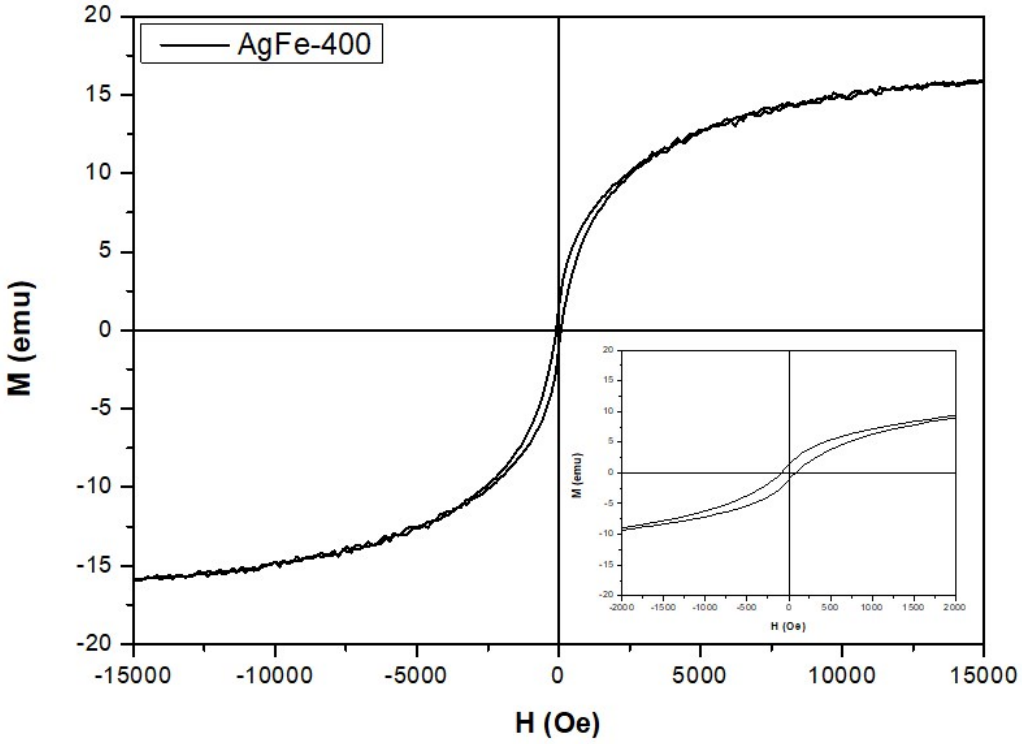

Fig. S22. Magnetic hysteresis loops of AgFe-400

(S1) J. Lee and S.-Y. Kwak, *Cryst. Growth Des*., **2017**, 17, 4496–4500